Fracture of Porous Ceramics: Application to the Mechanical Degradation of Solid Oxide Cell During Redox Cycling

A. Abaza[a], S. Meille[b], A. Nakajo[c], D. Leguillon[d], M. Hubert[a], C. Lenser[e], and J. Laurencin[a]

[a] Univ. Grenoble Alpes - CEA/LITEN, 17 Rue des martyrs, F-30854 Grenoble, France
[b] Univ. Lyon, INSA Lyon, UCBL, CNRS, MATEIS UMR 5510, 20 Av. A. Einstein, F-69621 Villeurbanne, France
[c] Ecole Polytechnique Fédérale de Lausanne, 1015 Lausanne, Switzerland
[d] Institut Jean le Rond d'Alembert, Sorbonne Université, Centre National de la Recherche Scientifique, UMR 7190, F-75005 Paris, France
[e] Institute of Energy and Climate Research – Materials Synthesis and Processing (IEK-1), Forschungszentrum Jülich GmbH, 52425 Jülich, Germany

A model based on the Phase Field approach has been developed to simulate the local fracture in porous electrode microstructures. The model capacity to predict the crack nucleation and propagation has been studied with theoretical considerations. For the validation, specific micro-compression tests have been performed on porous YSZ micro-pillars. As expected, the compressive fracture strength has been found to decrease with the material porosity. Moreover, a transition in the fracture mode has been detected from a brittle behavior toward a local damage when increasing the porosity. It has been shown that the model is able to reproduce correctly the experimental results. The validated model has been used to simulate the fracture of the YSZ backbone induced by the Ni re-oxidation in a typical Ni-YSZ cermet. The generation and localization of the micro-cracks have been discussed according to the degree of Ni re-oxidation and the local morphology of the electrode microstructure.

Introduction

Solid Oxide Cell (SOC) is a high-temperature electrochemical device that can be operated in both fuel and electrolysis modes. It is constituted of a dense electrolyte in Yttria Stabilized Zirconia (YSZ) sandwiched between two porous electrodes. The hydrogen electrode is classically made of a cermet composed of nickel (Ni) and YSZ (Ni-YSZ) (1,2). Because of system failures in operation (e.g. related to fuel shortage or to air re-introduction during the system shutdown), the nickel is liable to be re-oxidized inducing its volume expansion (3). The Ni swelling within the cermet generates high tensile stresses in the YSZ backbone leading to the apparition of micro-cracks (3). This mechanical damage of the ionic conducting phase within the cermet results in a substantial degradation of the overall cell performances (4-9). It is therefore required to further enhance the hydrogen electrode robustness for a higher redox tolerance. For this purpose, it is essential to predict accurately the formation and the distribution of micro-cracks in the YSZ network during Ni re-oxidation. Nevertheless, the accurate prediction of cracks nucleation and propagation in the complex microstructures of porous ceramics is still a subject of investigation. Moreover, there is a lack of data on fracture properties for the porous YSZ. In this frame, the mechanical characterization using uniaxial compression testing on micro-pillars has been carried out at different porosities considering two types of zirconia stabilized with 8% and 3% molar of Yttrium (i.e., 8YSZ and 3YSZ respectively). The experimental data have then been used to validate a model based on the Phase Field Method (PFM) applied to the fracture mechanics. Thanks to this validated model, the fracture of the YSZ backbone induced by the Ni re-oxidation has been simulated for a typical Ni-YSZ cermet. The generation and localization of the micro-cracks have been discussed according to the degree of Ni re-oxidation and the local morphology of the electrode microstructure.

Experiments

Sample Preparation

Samples with low and intermediate porosities were manufactured using a specific protocol. The preparation consisted to sinter pellets of compacted 8YSZ powders at different temperatures (i.e. 1270°C, 1230°C, 1200°C and 1150°C) for 1 hour under air. To produce samples with higher porosity, a typical Ni-8YSZ cermet was used by dissolving the nickel in HNO_3 acid at room temperature. Moreover, the same protocol was applied on a Ni-3YSZ cermet to obtain a highly porous 3YSZ material. Finally, it can be noticed that the study was complemented by the characterization of a fully dense 8YSZ membrane.

For each sample, a polished cross-section was observed by Scanning Electron Microscopy (SEM) to check the microstructure homogeneity and to estimate the sample porosity. For instance, the SEM images for the 8YSZ samples have revealed a homogenous microstructure with a higher porosity for the lower sintering temperature (Fig. 1). In addition, 3D reconstructions using the Focused Ion Beam – Scanning Electron Microscopy (FIB-SEM) tomography have been realized. On the one hand, the porosity has been measured on the 3D volumes to confirm the estimation obtained with the 2D images. On the other hand, the reconstructions have been used as inputs for the multiscale modeling approach.

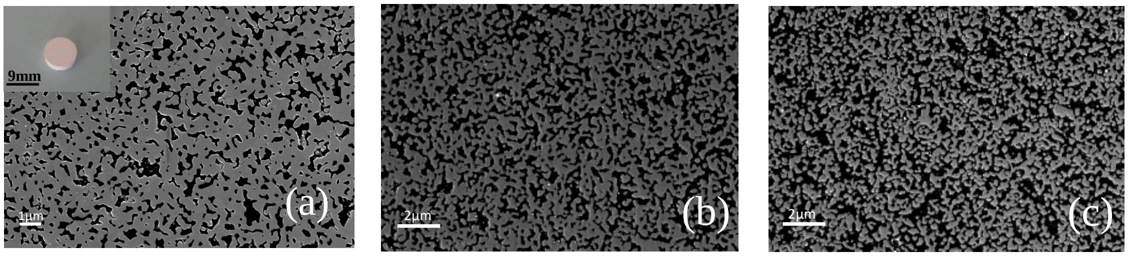

Fig 1. SEM observations of 8YSZ samples sintered at: a) 1270°C, b) 1230°C, c) 1150°C under air. The insert in Fig. 1a shows the pellet after sintering.

After manufacturing, the specimens for the mechanical characterizations were directly milled in the pellets using a Plasma Focused Ion Beam (PFIB) working with Xenon ions. The specimen were etched in the shape of micro-pillars for uniaxial micro-compression testing (Fig. 2a). In this frame, a special attention was paid to fulfil the geometrical recommendations regarding the specimen dimensions for a relevant test (9,10). Indeed, as shown in Fig. 2b, the micro-pillars present a nearly perfect axisymmetric geometry with a section of 60 µm ± 0.5. Moreover, the rule on the aspect ratio between the height of the pillar and the diameter, which is recommended to range between 2 and 3, was satisfied. Due to the Gaussian shape of the ion beam, the pillars were slightly tapered but a special attention was paid to limit the angle down to 6°. Finally, it has been checked by 3D reconstructions that the microstructure is not affected by the sample preparation (Fig. 2c).

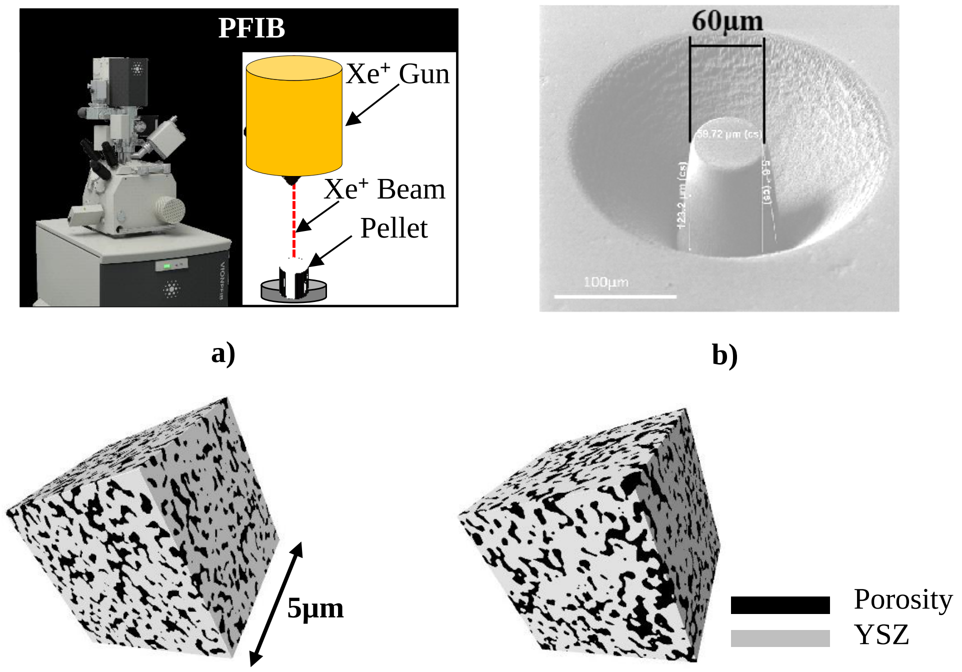

a) **b)**

3D reconstruction before the milling 3D reconstruction in the micro-pillar

c)

Fig 2. Procedure for the specimen preparation: a) Schematic representation of the Xenon PFIB used for the milling, b) micro-pillar obtained after milling, c) rendering volumes for the two reconstructed microstructures of the 8YSZ sample sintered at 1270 °C (in the pellet and the micro-pillar).

Mechanical Testing

The micro-compression test has been chosen as it generates a quasi-uniform stress field in the tested pillars. Moreover, this approach is well adapted to the characterization of thin cermet substrate used for the sample preparation (after Ni dissolution: cf. previous section). The micro-mechanical tests were performed using a nano-indenter associated with an optical microscope. Using the force-controlled mode, the pillars were compressed with a circular flat punch of 100 µm in diameter to measure the compression fracture strength of porous materials. For each investigated porosity, several pillars were tested. Around five tests were conducted up to the sample failure to identify the fracture strength. Other complementary experiments were stopped during the loading just before the sample collapse. For these specimens, the distribution of cracks within the microstructure has been carefully characterized on 2D FIB slice in order to assess the damage mode in the material. All the results are provided in Table I.

Results for Samples with Low and Intermediate Porosities. As an illustration, the typical stress-strain curves are provided in Fig. 3 for the 8YSZ samples sintered at different temperatures. As expected, a decrease of the fracture strength was found with decreasing the sintering temperature (i.e. by increasing the porosity). Indeed, the measured fracture strength was 1455±85 MPa, 950±5 MPa, 470±4 MPa and 125±5 MPa for the samples sintered at 1270°C,1230°C, 1200°C and 1150°C, respectively (Table I).

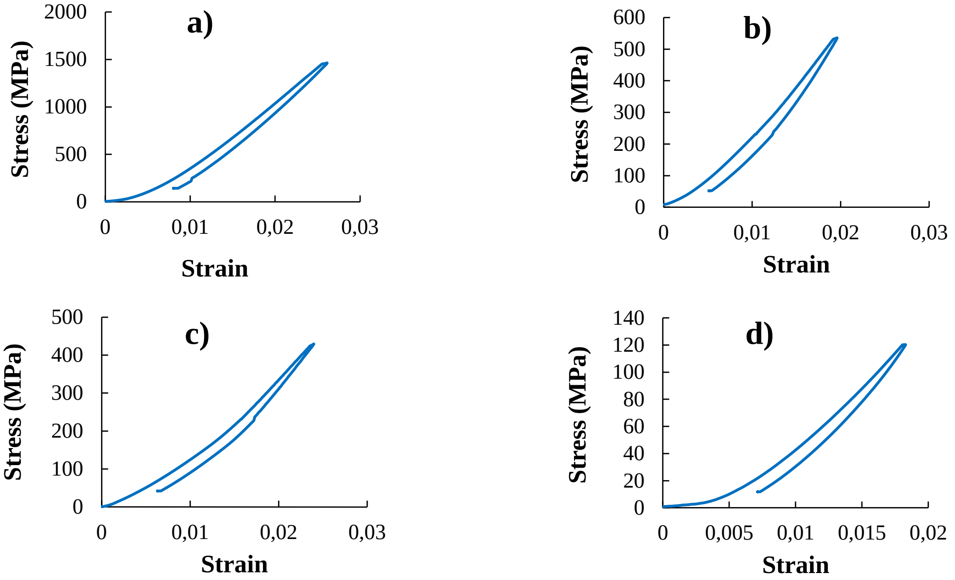

Fig 3. Stress-Strain curves of the 8YSZ samples sintered at: a) 1270°C, b) 1230°C, c) 1200°C, d) 1150°C. The tests were stopped before the fracture.

For the tested samples stopped just before the total failure of the pillars, the visualization of cracks in the microstructure has shown the presence of large cracks parallel to the loading direction (Fig. 4). These observations point out a brittle behavior for the 8YSZ at low and intermediate porosities (15).

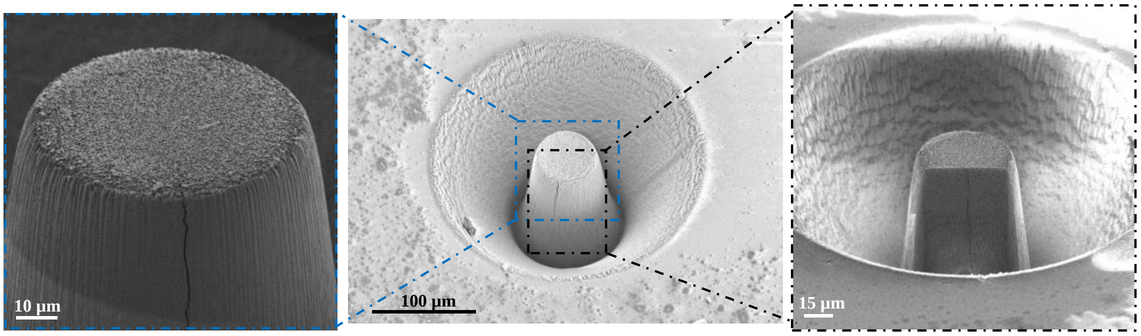

a)
b)
c)

Fig 4. Post-mortem characterization after the mechanical loading of the 8YSZ pillar sintered at 1270°C (low porosity): a) SEM image of a longitudinal macro-crack on the edge of the pillar, b) SEM image of the tested pillar, c) FIB-SEM cross section showing the large crack in the bulk of the pillar.

Results for Samples with High Porosities. The typical stress-strain curves recorded during the compression testing performed on the highly porous 8YSZ and 3YSZ samples (after Ni dissolution) are depicted in Fig. 5. For the 8YSZ material, the facture strength, which was estimated to 24±3 MPa, is consistent with the data measured on the 8YSZ pellets at low and intermediate porosities (Table I). Furthermore, as it could be anticipated, the compression strength for the highly porous 3YSZ is significantly higher than for 8YSZ. Indeed, a value of 154±20 MPa was measured in this case.

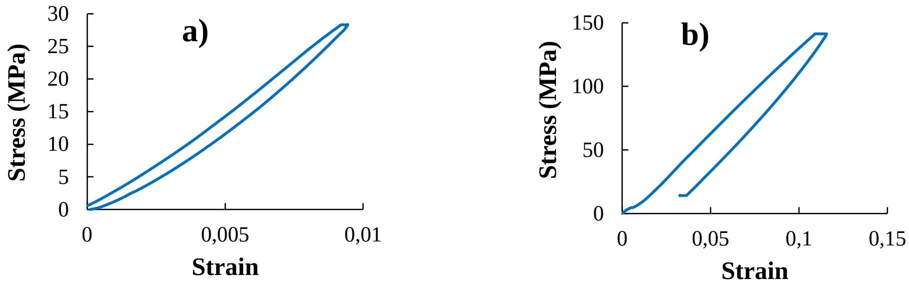

Fig 5. Stress-Strain curves of the highly porous samples: a) 8YSZ, b) 3YSZ.

The post mortem characterizations were also realized for the pillars tested just below the threshold leading to the complete failure. As shown in Fig. 6 for the 8YSZ and 3YSZ, a distribution of micro-cracks is detected in the bulk of the samples in the upper part of the pillar. This observation means that a diffuse damage is induced in the microstructure for these highly porous materials. Therefore, a transition has been highlighted from a brittle behavior at low and intermediate porosities towards a local damaging with micro-cracks at high porosity (15).

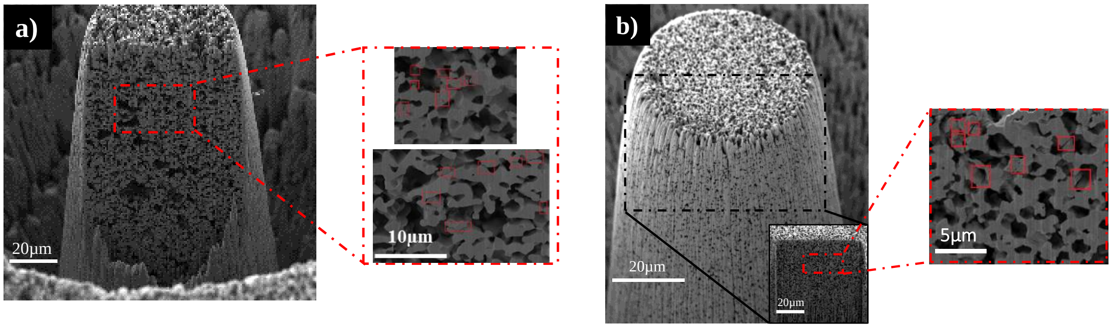

Fig 6. Post mortem characterization of the highly porous pillars after the mechanical loading with a zoom showing the micro-cracks in the bulk of the pillar (highlighted by red rectangles): a) 8YSZ, b) 3YSZ. The tests were stopped before the fracture.

The 8YSZ compressive fracture strength is plotted in Fig. 7 as a function of the porosity. A sharp decrease of the fracture strength can be observed for the porosity below ≈50% while a slighter evolution is found from 50% to 60%. It is worth noting that this transition is concomitant with the change in the fracture mode (Table I). Therefore, it can be proposed that the evolution of the fracture strength with the porosity is also dependent of the underlying mechanism controlling the rupture. All these experimental data have been used for the validation of the numerical model.

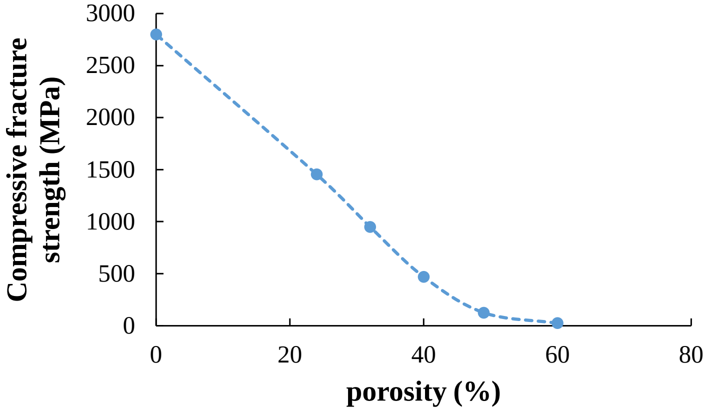

Fig 7. 8YSZ compressive fracture strength as a function of the porosity.

TABLE I. Results of the Mechanical Testing.

Material	Porosity (%)	Fracture strength (MPa)	Fracture mode
Highly porous 3YSZ	60	154	Local damaging
Highly porous 8YSZ	60	24	Local damaging
8YSZ-T1150°C	49	125	Brittle
8YSZ-T1200°C	40	470	Brittle
8YSZ-T1230°C	32	950	Brittle
8YSZ-T1270°C	24	1455	Brittle
Dense 8YSZ electrolyte	0	2800	Brittle

Modelling the fracture in porous electrodes

Model Description

The PFM approach has been selected to study the initiation and the growth of cracks in porous ceramics since it is mesh independent. The model is based on an diffuse description of the crack through a smooth scalar damage variable $\boldsymbol{d}$. This variable is referred as the phase field and can evolved from zero to one. The pristine material corresponds to $\boldsymbol{d} = 0$ while the total rupture is reached when $\boldsymbol{d} = 1$.The region of transition between the two states is controlled by a length scale parameter $\boldsymbol{\ell}$. Marigo et al. (11,13) were the first to propose a general theoretical framework for the development of this method on the basis of the Continuous Damage Mechanics (CDM). The key idea of their work is the reformulation of the fracture problem as the minimization of an energy functional without any additional criterion. In the present study, the implemented PFM is the one developed by Miehe et al. (14) allowing a robust staggered scheme for the numerical resolution. In this approach, the minimization of the energy functional is performed at a frozen damage for the phase-field (i.e. $\boldsymbol{d} = \boldsymbol{cte}$) leading to solve a 'classical' elastic problem:

$$\bar{\nabla} \cdot \bar{\bar{\boldsymbol{\sigma}}}(\bar{\bar{\boldsymbol{\varepsilon}}}, d) = 0 \text{ for the domain } V \text{ with } \bar{\bar{\boldsymbol{\sigma}}}.\bar{\boldsymbol{n}} = \bar{\boldsymbol{t}} \text{ on } \partial V \qquad [1]$$

Where $\bar{\bar{\boldsymbol{\sigma}}}$ and $\bar{\bar{\boldsymbol{\varepsilon}}}$ are the stress and the strain tensor respectively. The term $\bar{\boldsymbol{t}}$ is the applied force and $\bar{\mathbf{n}}$ is the outward normal applied on the domain surface ∂V.

Then, the resolution at a given loading (i.e. $\bar{\boldsymbol{u}} = cte$) yields the equation for the phase field computation when the crack propagates:

$$2(1-d)\mathcal{H} = \mathrm{G}_c\left(\frac{d}{\ell} - \ell\Delta d\right) \quad \text{with } \mathcal{H}(\bar{\boldsymbol{x}},t) = \max_{s\,\in\,[0,t]} \Psi^{+}(\bar{\boldsymbol{u}}(\bar{\boldsymbol{x}},t)) \qquad [2]$$

Where G_c is the critical energy release rate of the material. The term $\mathcal{H}$ is referred as an 'history' loading field taking into account the damage process irreversibility (14). It is expressed as the maximum of the energy component denoted Ψ^{+}. This term comes from the decomposition of the elastic strain energy into a component due to the tension (i.e. Ψ^{+}) and a component due to the compression (i.e. Ψ^{-}).

Evaluation of the Model Relevance to Study the Fracture in Porous Microstructure

It has been shown by many authors that the PFM model is able to simulate accurately the propagation, the branching and the multi-cracking problem in complex geometry (15). Nevertheless, there is still a controversy on the PFM capacity to accurately predict the crack nucleation. Indeed, it has been proposed that the length scale parameter $\boldsymbol{\ell}$ could be linked to the Irwin length and thus related to the physical properties controlling the crack initiation (i.e. fracture strength and toughness) (16-18). In this condition, the PFM approach should constitute a relevant method to model the crack nucleation. However, some other authors have also claimed that $\boldsymbol{\ell}$ is just a numerical parameter without any physical meaning (19). In this context, a special attention has been paid to interpret the real nature of $\boldsymbol{\ell}$ and to evaluate the model capability to accurately predict the crack nucleation. For this purpose, the PFM simulations have been compared to the results given by the validated mixed criterion proposed by Leguillon (20). This part of the study has been conducted for an ideal V-notched sample and a crack blunted by a cavity. Afterwards, the model has been applied to simulate the crack initiation and propagation in representative porous microstructures. It is worth noting that all the simulations have been carried out in the 2D plane strain assumption considering a symmetrical three-point bending test.

V-notched Sample. The geometry of the implemented V-notched sample with different opening angles 2β is depicted in Fig. 8a (i.e. $\boldsymbol{\beta} \in \{\mathbf{30°},\ \mathbf{45°}, \mathbf{60°}\}$). In this case, the crack is initiated from the stress singularity induced by the V-notch tip. A typical force-displacement curve simulated with the PFM is shown in Fig. 8b. It can be noticed that the force is progressively increased up to reach a critical loading $\boldsymbol{P_c}$ corresponding to the fracture initiation. The apparent fracture toughness $\boldsymbol{K}_{\mathbf{Ic}}^{\mathbf{app}}$ is then calculated from the maximum loading using the following equation (21):

$$K_{\mathrm{Ic}}^{\mathrm{app}} = \left(\frac{3P_{\mathrm{c}}L}{2bh^2}\right) h^{(1-\lambda)} f\left(\frac{a}{h}\right) \qquad [3]$$

Where $\boldsymbol{f}\left(\frac{\boldsymbol{a}}{\boldsymbol{h}}\right)$ is a dimensionless factor taken from (21), $\boldsymbol{b}$ is the beam thickness fixed to the unity for the 2D simulations and $\boldsymbol{\lambda}$ is the singularity order calculated using the equation reported in (21). The evolution of the fracture toughness deduced from the PFM simulations has been evaluated for the 8YSZ material as a function of the opening angle. This result has been obtained with an *ad hoc* value of the length scale parameter denoted

$\boldsymbol{\ell_{8YSZ}}$. The results have been compared to the prediction given by the mixed criterion in (Fig. 8c). It can be seen that the two curves are quite perfectly superimposed. The PFM can thus reproduce the increase of the apparent fracture toughness with increasing the opening angle. This evolution involves a change in the criterion controlling the initiation (20). Indeed, for small opening angles (i.e. β = 30°), the crack nucleation is mostly governed by an energy criterion whereas both energy and stress criteria are involved for larger angles. It can be noticed that the same study has been performed considering the 3YSZ material (paper under preparation). In this case, it has been found that the evolution of the apparent fracture toughness with the notch-opening angle can be also retrieved by the PFM method considering a length scale parameter for the 3YSZ ($\boldsymbol{\ell_{3YSZ}}$). Besides, a relation has been highlighted between these parameters of the phase field and the Irwin characteristic lengths. From this analysis, it has been shown that the PFM is able to predict the crack onset from a stress singularity.

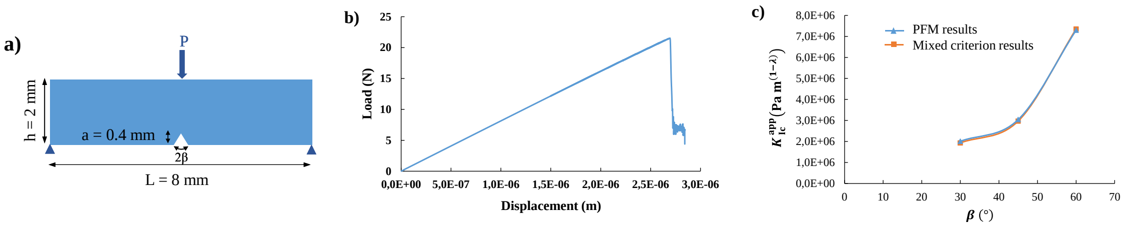

Fig 8. Three point bending test on a V-notched sample: a) implemented geometry b) Load/Displacement curve for 8YSZ material and β = 60 °, c) comparison between PFM and mixed criterion results for 8YSZ material.

<u>Crack Blunted by a Cavity.</u> The same analysis has been carried out by a crack blunted by a cavity of different radii (Fig. 9a). In this configuration, the crack is initiated from the stress concentration induced by the pore associated with the macro-crack. For this geometry, the apparent fracture toughness $K_{\mathrm{Ic}}^{\mathrm{app}}$ is related to the critical loading P_c calculated with the PFM method as follows (22):

$$K_{\mathrm{Ic}}^{\mathrm{app}} = \left(\frac{P_{\mathrm{c}}}{b\sqrt{h}}\right) f\left(\frac{a}{h}\right) \qquad [4]$$

Where $f\left(\frac{a}{h}\right)$ is a dimensionless factor taken from (22). The computed relative toughness (i.e. $R = K_{\mathrm{Ic}}^{\mathrm{app}}/K_{\mathrm{Ic}}$) has been plotted as a function of the pore radius in Fig. 8b. It has been found that the PFM simulations are in good agreement with the predictions of the mixed criterion. Indeed, the PFM is able to retrieve the increase of the apparent toughness with the cavity size (23). This strengthening effect is due to the blunting of the crack leading to a relative toughness R higher than unity. All these statements show that PFM model is also able to predict the crack nucleation from a stress concentration. It is worth noting that these results have been obtained for a value of ℓ different from the one used in the configuration of the V-notched sample. Therefore, this parameter is not only dependent on the material properties but also on the local geometry where the crack initiates (paper under preparation).

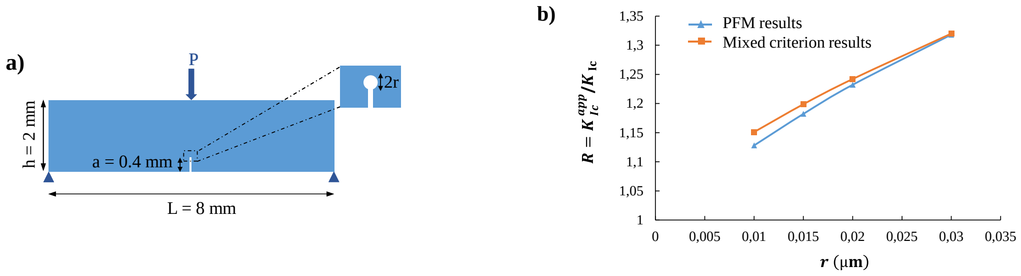

Fig 9. Three point bending test on a sample with a crack blunted by a cavity: a) implemented geometry, b) comparison between PFM and mixed criterion results for 8YSZ material.

Crack Initiation in Porous Microstructures. In complementarity with the previous ideal geometries, the capacity of the PFM to simulate the fracture in porous microstructures has been checked. For this purpose, the simulated domain is described by a porous medium as depicted in Fig. 10a. The microstructures have been generated using the Gaussian random field model. Indeed, this method provides numerical 3D microstructures that mimic accurately the morphology of the real electrodes (24). In this study, 2D slices with similar microstructural characteristics (i.e. same phase volume fraction and characteristic length) have been extracted from the generated 3D volume. In order to address the impact of porosity on the fracture toughness, microstructures with different porosities $\boldsymbol{\varepsilon} \in \{\mathbf{10}\%,\ \mathbf{20}\%, \mathbf{30}\%\}$ have been considered. The study has been conducted for the 3YSZ material for which experimental data are available in literature (25). It can be noticed that the relation [4] has been used to express the apparent toughness as a function of the critical loading calculated with the PFM. The evolution of $\boldsymbol{K}_{\mathbf{Ic}}^{\mathbf{app}}$ with the porosity is shown in Fig. 10b. It can be remarked that the phase field predictions catch the decrease of the apparent fracture toughness with the porosity increase. Moreover, a slight variation of the predicted $\boldsymbol{K}_{\mathbf{Ic}}^{\mathbf{app}}$ has been found for the two simulated slices taken from the 3D microstructure (Fig. 9b). This result is explained by the local variation of the computed microstructure at the crack tip. Moreover, a quite good agreement has been found with the experimental data. Indeed, even if the predicted toughness is higher than the experimental one, the evolutions of the two curves with the porosity are similar. The difference in the absolute value of the measured and simulated toughness could be explain by the 2D assumption and by the synthetic microstructures, which are not exactly the same than the tested ones. Nevertheless, from this analysis, it can be concluded that the PFM model is well adapted to study the fracture in the porous microstructures.

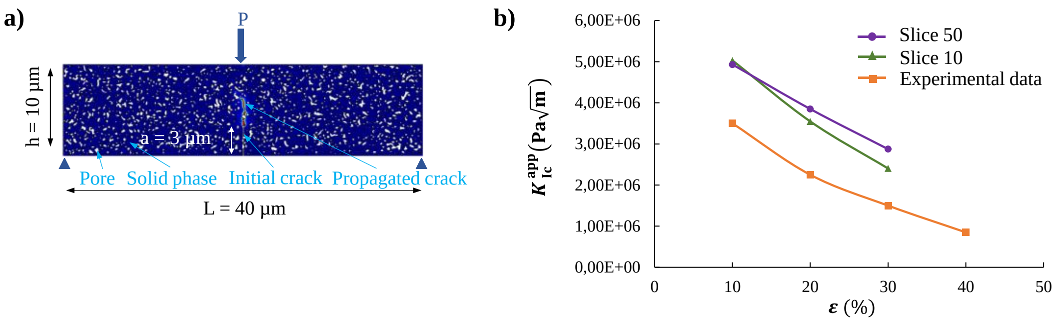

Fig 10. Three point bending test on a porous microstructure: a) implemented geometry, b) the evolution of the apparent fracture toughness with the porosity for two different slices of the generated 3D microstructures.

Multiscale Approach and Model Validation

For a complete validation of the phase field method, the experiments reported in the previous section has been modelled using a multiscale approach. For this purpose, the compression test has been simulated in 2D taking advantage of the axisymmetric geometry of the micro-pillars (Fig. 11a). An equivalent homogenous medium has been considered for the simulations for which the effective elastic properties have been computed by homogenization on the 3D reconstructions (26). The macroscale simulations for the whole micro-pillars has allowed providing the displacements, which have been applied as boundary conditions on the edge of a 3D microstructure (Fig. 11b). It can been noticed that the simulated volume is located in the upper part of the pillar where the stresses are the highest. The distribution of the principal stresses in the microstructure is given in Fig. 11c for an applied compressive displacement on the micro-pillar of 2.8 µm. As expected, some parts of the YSZ network are submitted to a non-negligible tensile stress (Fig. 11b). Therefore, these regions will constitute zones where the cracks are liable to nucleate. To analyze this possibility, the PFM model has been applied. Although the study is still on going, the preliminary results have shown that the method is able to reproduce the decrease of the compressive fracture strength with the porosity as experimentally observed in Fig. 7. Therefore, the phase field model appears as a relevant numerical to study the fracture in the 3D electrode microstructure.

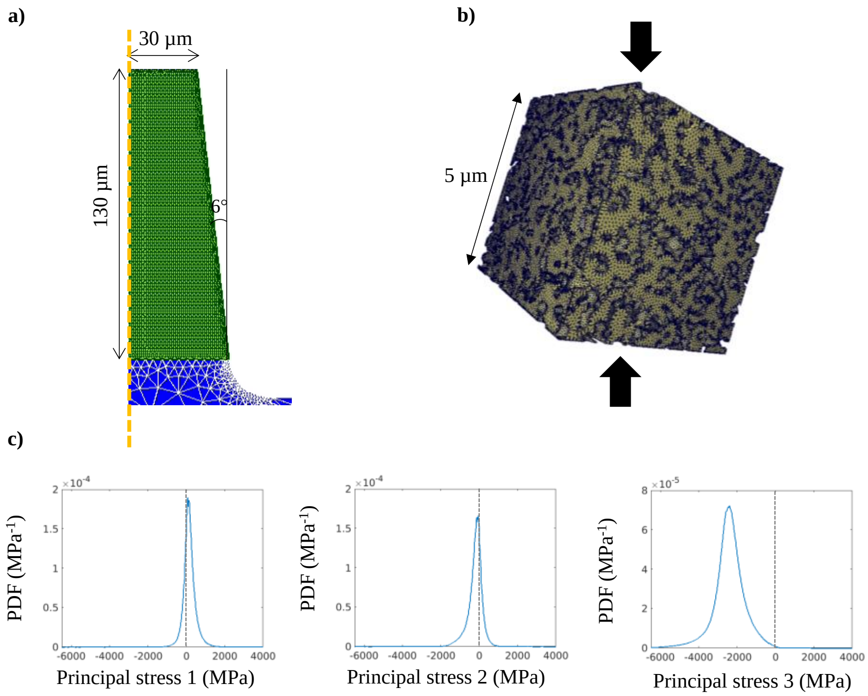

Fig11. Multiscale approach: a) axisymmetric geometry of the micro-pillar, b) porous YSZ microstructure under compression, c) probability density function (PDF) of the principal stresses.

YSZ Fracture During Ni Re-oxidation

After the PFM model validation, the local damage within the YSZ backbone induced by the Ni re-oxidation has been addressed. For this purpose, the initial implemented model has been extended to take into count the Ni expansion during re-oxidation. In this objective, the Ni swelling has been simulated through a thermal dilatation as follows:

$$\bar{\bar{\varepsilon}}_{th} = \alpha_{th}\left(T - T_{ref}\right) \qquad [4]$$

Where $\boldsymbol{\alpha_{th}}$is the thermal expansion coefficient for Ni. The temperature difference ($\boldsymbol{T - T_{ref}}$) has been chosen in such a way that the thermal strain $\boldsymbol{\bar{\bar{\varepsilon}}_{th}}$ can reproduce the Ni volume expansion. It is worth noting that the coefficient for YSZ has been set to zero to avoid the dilation of this phase during the simulation. Besides, it has been shown in (3) that the complete re-oxidation of the Ni is reached for a volume increase of 70%. Thus, a degree of Ni re-oxidation can be affected to each Ni volume expansion. In this study, PFM simulations have been conducted on a Ni-YSZ volume of 2 µm^3 (Fig. 12). It has been found that the first crack is created in the YSZ network when the degree of Ni re-oxidation reaches a critical value of around 11% (Fig. 12). These results means that the damage in the ceramic occurs almost at the early stage of the Ni re-oxidation. Therefore, even before the catastrophic rupture of the electrolyte in the cell (triggered for a degree of re-oxidation of around 60-65% at 800°C (27)), the cermet is subjected to an internal damage that will decrease the cell performances. Finally, it can be observed in Fig. 12 that the first crack has been generated into a thin YSZ ligament surrounded by Ni. This ligament was thus submitted to a high tensile stress during the re-oxidation. Therefore, the local fracture in the YSZ is highly sensitive to the local morphology of the cermet. From this point of view, the developed PFM approach is a powerful method to analyze the role of the microstructure on the electrode robustness.

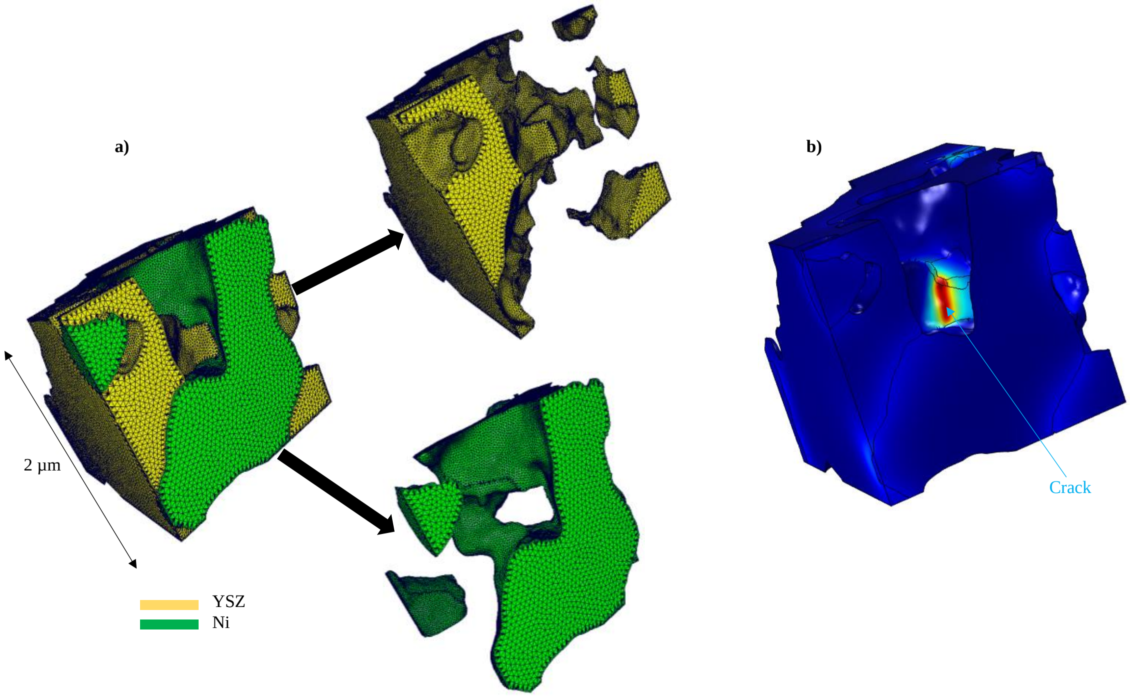

Fig 12. Simulation of the fracture induced by the Ni re-oxidation: a) 3D reconstruction of a Ni-YSZ cermet, b) visualization of the resulting crack.

Conclusion

Micro-compression tests have been performed on porous YSZ micro-pillars tested over a large range of porosities. It has been found that the compressive fracture strength is decreased with increasing the pore volume fraction. The tested samples have been carefully characterized to assess the damage in the microstructure. A transition has been observed from a brittle behaviour at low porosity (bellow 50%) towards a local damage at high porosity. All these experimental data have been used to validate a numerical model based on the Phase Field Method (PFM) to simulate the local damage in the 3D microstructure. The relevance of this model to accurately predict the crack nucleation in porous material has been previously confirmed with theoretical considerations. In this frame, it has been shown that the simulations with the PFM model are in good agreement with the theoretical prediction given by the mixed criterion. In addition, it has been checked that the PFM model is able to accurately simulate the expected decrease of the fracture toughness with the porosity increase. As a final validation, it has been shown that the evolution of the experimental compressive fracture strength with porosity is well captured by the model. The PFM approach has been then applied to study the local rupture in the YSZ backbone induced by the Ni re-oxidation. It has been found that the first cracks can be generated even for a very low degree of Ni oxidation.

Acknowledgments

This project has received funding from the Fuel Cells and Hydrogen 2 Joint Undertaking (JU) under grant agreement n° 825027 (AD ASTRA project). The JU receives support from the European Union’s Horizon 2020 research and innovation program and Denmark, France, Italy, Spain, Poland, Netherlands, Greece, Finland, Estonia, Germany, United Kingdom, Switzerland.

References

1. S. P. Jiang and S. H. Chan, *Journal of Materials Science*, **39**, 4405–4439 (2004).
2. N. H. Menzler, F. Tietz, S. Uhlenbruck, H. P. Buchkremer, and D. Stöver, *J Mater Sci*, **45**, 3109–3135 (2010).
3. A. Faes, A. Nakajo, A. Hessler-Wyser, D. Dubois, A. Brisse, S. Modena and J. Van herle, *Journal of Power Sources*, **193**, 55–64 (2009).
4. A. Faes, A. Hessler-Wyser, A. Zryd, and J. Van herle, *Membranes*, **2**, 585–664 (2012).
5. D. Sarantaridis, R. A. Rudkin, and A. Atkinson, *Journal of Power Sources*, 7 (2008).
6. S. Sukino, S. Watanabe, K. Sato, F. Iguchi, H. Yugami, T. Kawada, J. Mizusaki and T. Hashida, *ECS Trans.*, **35**, 1473–1482 (2019).
7. T. Klemensø, C. Chung, P. H. Larsen, and M. Mogensen, *Journal of The Electrochemical Society*, **152**, 2186-2192 (2005).
8. J. Laurencin, G. Delette, B. Morel, F. Lefebvre-Joud, and M. Dupeux, *Journal of Power Sources*, **192**, 344–352 (2009).

9. A. W. Colldeweih, A. Baris, P. Spätig, and S. Abolhassani, *Materials Science and Engineering: A*, **742**, 842–850 (2019).
10. H. Zhang, B. E. Schuster, Q. Wei, and K. T. Ramesh, *Scripta Materialia*, **54**, 181–186 (2006).
11. G. A. Francfort and J.-J. Marigo, *Journal of the Mechanics and Physics of Solids*, **46**, 1319–1342 (1998).
12. K. Pham and J.-J. Marigo, *Comptes Rendus Mécanique*, **338**, 199–206 (2010).
13. K. Pham and J.-J. Marigo, *Comptes Rendus Mécanique*, **338**, 191–198 (2010).
14. C. Miehe, M. Hofacker, and F. Welschinger, *Computer Methods in Applied Mechanics and Engineering*, **199**, 2765–2778 (2010).
15. T. T. Nguyen, J. Yvonnet, M. Bornert, C. Chateau, F. Bilteryst and E. Steib, *Extreme Mechanics Letters*, **17**, 50–55 (2017).
16. E. Tanné, T. Li, B. Bourdin, J.-J. Marigo, and C. Maurini, *Journal of the Mechanics and Physics of Solids*, **110**, 80–99 (2018).
17. H. Amor, J.-J. Marigo, and C. Maurini, *Journal of the Mechanics and Physics of Solids*, **57**, 1209–1229 (2009).
18. M. J. Borden, C. V. Verhoosel, M. A. Scott, T. J. R. Hughes, and C. M. Landis, *Computer Methods in Applied Mechanics and Engineering*, **217–220**, 77–95 (2012).
19. A. Kumar, B. Bourdin, G. A. Francfort, and O. Lopez-Pamies, *Journal of the Mechanics and Physics of Solids*, **142**, 104027 (2020).
20. D. Leguillon, *European Journal of Mechanics - A/Solids*, **21**, 61–72 (2002).
21. M. L. Dunn, W. Suwito, and S. Cunningham, *International Journal of Solids and Structures*, **34**, 3873–3883 (1997).
22. T.L. Anderson, *Fracture mechanics: fundamentals and applications*, p. 688, Taylor & Francis Group, Florida, (2005).
23. D. Leguillon and R. Piat, *Engineering Fracture Mechanics*, **75**, 1840–1853 (2008).
24. H. Moussaoui, J. Laurencin, Y. Gavet, G. Delette, P. Cloetens, T. Le Bihan and J. Debayle, *Computational Materials Science*, **143**, 262–276 (2018).
25. P. Khajavi, J. Chevalier, P. Vang Hendriksen, J-W. Tavacoli, L. Gremillard and H. Lund Frandsen, *Journal of the European Ceramic Society*, **40**, 3191–3199 (2020).
26. G. Delette, J. Laurencin, F. Usseglio-Viretta, J. Villanova, P. Bleuet, E. Lay-Grindler and T. Le Bihan, *International Journal of Hydrogen Energy*, **38**, 12379–12391 (2013).
27. J. Laurencin, V. Roche, C. Jaboutian, I. Kieffer, J. Mougin and M.C. Steil, *International Journal of Hydrogen Energy*, **37**, 12557–12573 (2012).